An evaluation of the mass and power scaling of synthetic jet actuator flow control technology for civil transport aircraft applications

W J Crowther* and **L T Gomes**
School of Mechanical, Aerospace and Civil Engineering, University of Manchester, Manchester, UK

The manuscript was received on 7 November 2007 and was accepted after revision for publication on 7 April 2008.

DOI: 10.1243/09596518JSCE519

Abstract: This paper aims to develop understanding of the systems costs associated with the application of flow control systems to civil transport aircraft based on the use of electrically powered synthetic jet actuators (SJAs). The study is based on the development of a low-order mass model using estimated power specific masses of generation, management, distribution, and conversion subsystems; application of existing empirical rules for application of pneumatic boundary layer mixing flow control devices to determine the required fluid power for an A320 case study application; and characterization and optimization of lab-based SJA technology to establish realistic estimates for power conversion efficiency and actuator maximum authority. The peak velocity obtained from a velocity-optimized synthetic jet actuator was 130 m/s, at a corresponding power efficiency of 7 per cent. The highest power efficiency obtained was 14 per cent, corresponding to a peak velocity of 70 m/s. The power specific mass for the overall flow control system considered for the A320 application is estimated to be around 1 kg of system mass per kW of electrical power required, of which around 50 per cent is due to power generation and 30 per cent is due to power conversion (actuation).

Keywords: synthetic jet actuator, flow control, aircraft systems, mass, power

1 INTRODUCTION

Current generation civil transport aircraft are based on evolutionary development of basic designs established in the 1950s, and, historically, most improvements in aerodynamic performance have come through continued refinement of the aircraft external geometry. This process is now highly mature, and therefore further aerodynamic gains from geometric optimization alone are becoming increasingly non-cost-effective to achieve [**1**]. Aircraft designers are therefore looking for alternative approaches to unlocking improved aerodynamic performance that do not depend on increasingly complex geometries. One such approach is offered by flow control.

**Corresponding author: School of Mechanical, Aerospace and Civil Engineering, University of Manchester, Manchester M60 1QD, UK. email: w.j.crowther@man.ac.uk*

Flow control may be defined as the beneficial modification of a fluid flow over a surface of fixed geometry through the targeted introduction of energy or effort. The primary mechanism by which most flow control actuators work is that of introduction and/or redistribution of momentum within a fluid flow. Passive flow control actuators such as vane vortex generators introduce angular momentum into a flow using energy extracted from the mean flow, whereas active devices introduce momentum into a flow using energy from an external power source.

Fluid injection devices may be powered by generating fluid power centrally, e.g. from a conventional pump or compressor, and distributing this power to local actuators via a pipe network, or by generating fluid power locally from an electrical supply at the actuator. Central fluid power generation is energetically efficient, but there are considerable losses associated with distributing this power to the actuators, and considerable mass and volume

penalty associated with the piping required. Local fluid power generation will generally be less efficient than central generation due to the requirement for generation of multiple small amounts of power. However, the distribution of electrical power to multiple actuators can be made very much more efficient in terms of reduced energy losses and system mass compared to the equivalent fluid power distribution network.

Synthetic jet actuators (SJAs) are a class of momentum injection flow control actuators that lend themselves to electric operation, and have been widely studied in the literature [**2**]. In this type of actuator, electrical power is converted into fluid power via the mechanical excitation of an oscillating diaphragm on one or both sides of a chamber. Fluid is able to enter and exit the chamber via an orifice, and under steady state operation the net mass flux through the orifice is zero. However, due to asymmetry in the boundary conditions for suction and expulsion at the orifice exit, the device produces a positive net flow of momentum into the surroundings, and hence provides an actuation input to an adjacent flow.

There are many studies in the literature looking at the potential performance benefits of flow control in general and SJA applications in particular. However, due to the cost and complexity of undertaking flow control experiments or calculations at industrial scale, most of these studies tend to focus on the more fundamental fluid mechanics aspects [**3–12**]; there is therefore currently little reliable information on the overall performance benefit to a complete aircraft. In order to move the debate forwards, the present study focuses on careful evaluation of the cost side of the overall performance evaluation, which is presently a more tractable problem. Given information from this study, it is then possible to establish the minimum performance benefit necessary from a flow control system in order for the overall system to *break even*, i.e. the point at which further improvements in performance can start to have a positive spiral effect on the overall aircraft design.

The system model used as the context for the present work is shown in Fig. 1. The domain of interest covers the overall process of converting chemical energy from fuel into useful fluid power delivered by a flow control actuator.

The rest of the paper is organized as follows. Section 2 introduces a low-order mathematical model of a generic electrically powered flow control system, and defines the model inputs, outputs, and parameters used in the present study. Section 3 describes the experimental apparatus used to obtain quantitative data on the performance of geometrically optimized synthetic jet hardware for input into the flow control system model, and defines the method used for the application of the model to a case study analysis. Results from the experimental work and case study analysis are presented in section 4, followed by conclusions in section 5.

2 MATHEMATICAL MODEL FOR ESTIMATING FLOW CONTROL SYSTEM POWER AND MASS

The fluid mechanics underpinning the proposed flow control system model is based on empirical data on the performance of momentum injection devices used for separation control applications. A simple dimensional analysis of the problem suggests that the interaction of a jet in a cross flow is defined by the following dimensionless parameters

$$\text{Ratio of orifice diameter to local boundary layer height} = \Delta = \frac{d}{\delta} \tag{1}$$

$$\text{Ratio of actuator spanwise spacing to orifice diameter} = \lambda = \frac{\ell}{d} \tag{2}$$

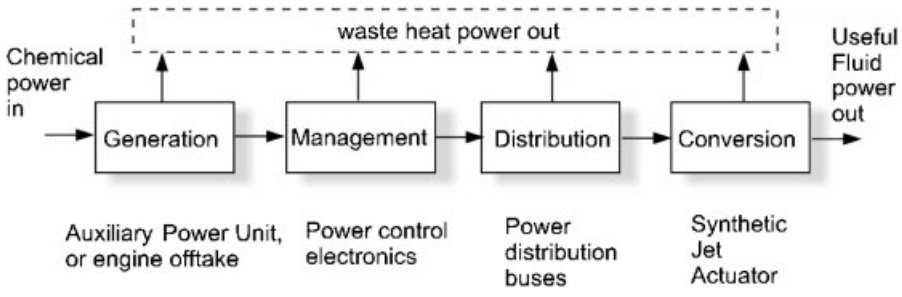

Fig. 1 Schematic illustration of the energy flow path for an electrically powered momentum injection flow control system

Ratio of peak jet velocity to local free stream velocity $= V_R = \dfrac{\hat{U}_j}{U_L}$ (3)

Empirical evidence suggests that for both effectiveness and efficiency, typical values for the above dimensionless parameters are $\Delta \cong 0.2$, $\lambda \cong 10$, and $V_R \cong 1$ [**6**].

It is assumed that the flow control application is based on the deployment of a single row of momentum injection actuators at a given streamwise location on a body (most likely a wing). To establish the fluid power requirements for a particular case, it is first necessary to estimate the local free stream velocity, density, and boundary layer height at the location where the flow control is applied, and also to define the array spanwise (cross stream) extent. Given the empirical ratios defined in the paragraph above, values for the orifice diameter, jet peak velocity, and number of orifices can be obtained. In terms of applicability of the model as part of a case study analysis, the local air density will be defined by altitude and the local free stream velocity for a particular application can be easily obtained from an estimate of the local pressure coefficient. Estimation of the local boundary layer height can be obtained via use of commonly available viscous coupled panel method tools such as JavaFoil [**13**]. However, for the present work, the boundary layer was estimated from a zero pressure gradient turbulent flat plate model [**14**]

$$\delta = 0.383\left(\frac{\nu}{U_L}\right)^{1/5} x^{4/5} \tag{4}$$

where ν is the kinematic viscosity, U_L is the local free stream velocity, and x is the distance downstream from the leading edge of the plate.

The mean fluid power delivered by a total of n actuator orifices is by definition

$$W_F = \frac{1}{2} n \rho A \overline{U}_j^3 \tag{5}$$

where A is the orifice area and $\overline{U}_j^3$ is the time average of the cube of the velocity. If the velocity from the actuator is measured at one orifice diameter above the orifice, then it is reasonable to approximate the time-varying velocity as a biased sinusoid such that the peak velocity is equal to $\hat{U}_j$ and the minimum velocity is equal to zero, that is

$$U_j(t) = \frac{\hat{U}_j}{2}(1 - \cos \omega t) \tag{6}$$

The time average cube of this velocity is then given by

$$\overline{U}_j^3 = \frac{1}{T}\int_0^T \left[U_j(t)\right]^3 dt = \frac{5}{16}\hat{U}_j^3 \cong \frac{1}{3}\hat{U}_j^3 \tag{7}$$

Using the dimensionless parameters defined in equations (1) and (2), the number n of actuators required for a given boundary layer height δ and spanwise extent of array s_A is given by

$$n = \frac{s_A}{\lambda \delta \Delta} \tag{8}$$

Substitution of equations (3) and (8) into the equation for required power (equation (5)) and use of the expression for the mean cube of velocity (equation (7)) gives the following expression for the required fluid power for a given flow control application

$$W_F = \frac{\pi}{12}\frac{V_R^3 \Delta}{\lambda}\frac{1}{2}\rho s_A \delta U_L^3 \tag{9}$$

The grouping $\frac{1}{2}\rho s_A \delta U_L^3$ represents the equivalent free stream power passing across an area defined by the span of the actuator array and the local height of the boundary layer, and the grouping $(\pi/12)(V_R^3\Delta/\lambda)$ represents the fraction of the equivalent free stream power that is delivered by the actuators. For the dimensionless parameter values used in the present study, the 'power fraction' is approximately 0.01; i.e. the actuators are delivering approximately 1 per cent of the equivalent free stream power in the boundary layer.

By definition, the electric–fluid power conversion efficiency of the actuators, η, represents the fraction of electric power transformed into fluid power, and is defined as $\eta = W_F/W_E$. The electrical power is defined as

$$W_E = \frac{1}{T}\int_0^T V(t) I(t) dt \tag{10}$$

where $V(t) = (V_0/2)\sin(\omega t)$ is the sinusoidal voltage driving the actuator, $I(t)$ is the current, and T is the period.

To determine the overall mass of the system required to deliver a given amount of fluid power,

it is assumed that for each of the subsystems identified in Fig. 1 there is a known power efficiency and that the mass of each subsystem can be modelled using a single power specific mass parameter that enables the mass to be scaled for different power requirements. The model inputs, outputs, and parameters described above are summarized in Table 1.

A mathematical model for the system is derived as follows. The power output from each of the subsystems defined in Fig. 1 is, by definition, given by

$$\begin{aligned} W_{\mathrm{g}} &= \eta_{\mathrm{g}} W_{\mathrm{Ch}} \\ W_{\mathrm{m}} &= \eta_{\mathrm{m}} W_{\mathrm{g}} \\ W_{\mathrm{d}} &= \eta_{\mathrm{d}} W_{\mathrm{m}} \\ W_{\mathrm{F}} &= \eta_{\mathrm{c}} W_{\mathrm{d}} \end{aligned} \tag{11}$$

The mass of each of the subsystems is then given by

Table 1 Flow control system model definition: inputs, outputs, and parameters

Model inputs	
δ	Local boundary layer height at point of application (m)
U	Local free stream velocity at point of application (m/s)
ρ	Local air density at point of application (kg/m^3)
x, s_{A}	Chordwise and spanwise extent of flow control array (m)
Δt	Required duration of operation (s)
Model outputs	
d, D_{o}	Orifice diameter (m)
n	Number of orifices
W_{E}	Overall system electrical power requirement (W)
m	Overall system mass (kg)
Model parameters	
Fluid dynamics	
Δ	Ratio of actuator orifice diameter to local boundary layer height
λ	Ratio of orifice spacing to orifice diameter
V_{R}	Ratio of actuator exit velocity to local free stream velocity
System hardware	
η_{g}	Power generation efficiency = 1.0
η_{m}	Power management efficiency = 1.0
η_{d}	Power distribution efficiency = 1.0
η_{c}	Power conversion efficiency = 1.0
$m_{W_{\mathrm{g}}}$	Power generation specific mass (kg/kW)
$m_{W_{\mathrm{m}}}$	Power management specific mass (kg/kW)
$m_{W_{\mathrm{d}}}$	Power distribution specific mass per unit length (kg/kW m)
$m_{W_{\mathrm{c}}}$	Power conversion specific mass (kg/kW)
$\dot{m}_{W_{\mathrm{g}}}$	Power generation specific fuel mass flowrate (kg/kW s)

$$\begin{aligned} m_{\mathrm{g}} &= m_{W_{\mathrm{g}}} W_{\mathrm{g}} \\ m_{\mathrm{m}} &= m_{W_{\mathrm{m}}} W_{\mathrm{m}} \\ m_{\mathrm{d}} &= m_{W_{\mathrm{d}}} W_{\mathrm{d}} \\ m_{\mathrm{c}} &= m_{W_{\mathrm{c}}} W_{\mathrm{F}} \end{aligned} \tag{12}$$

where $m_{W_{\mathrm{g}}}$, $m_{W_{\mathrm{m}}}$, $m_{W_{\mathrm{d}}}$, $m_{W_{\mathrm{c}}}$ are power-specific mass parameters representing the mass cost of hardware per unit power flow through a subsystem.

There is also a mass associated with the total mass of fuel used for a given duration of operation of the flow control system. This is given by

$$m_{W_{\mathrm{fuel}}} = \dot{m}_{W_{\mathrm{g}}} W_{\mathrm{g}} \Delta t \tag{13}$$

where $\dot{m}_{W_{\mathrm{g}}}$ is a power specific fuel consumption for the generator and Δt is the duration of operation.

Since the energy losses in the system are dominated by losses during electric to fluid power conversion in the actuator, it was decided for reasons of simplicity in the present study to set all power efficiency terms apart from η_{c} to unity, that is

$$\eta_{\mathrm{g}} = \eta_{\mathrm{m}} = \eta_{\mathrm{d}} = 1$$

This simplifies equation (11), giving the overall required electrical power as

$$W_{\mathrm{E}} = W_{\mathrm{g}} = W_{\mathrm{m}} = W_{\mathrm{d}} = \frac{W_{\mathrm{F}}}{\eta_{\mathrm{c}}} \tag{14}$$

The resulting model for the mass of the overall system is now given by

$$m = \frac{W_{\mathrm{F}}}{\eta_{\mathrm{c}}} \left[m_{W_{\mathrm{g}}} + m_{W_{\mathrm{m}}} + m_{W_{\mathrm{d}}} + m_{W_{\mathrm{c}}} + \dot{m}_{W_{\mathrm{g}}} \Delta t \right] \tag{15}$$

Note that the distribution specific mass $m_{W_{\mathrm{d}}}$ will in practice depend on the distance between generation and conversion systems. To accommodate this, a power specific mass per unit length $m'_{W_{\mathrm{d}}}$ is defined such that

$$m_{W_{\mathrm{d}}} = m'_{W_{\mathrm{d}}} l \tag{16}$$

where l is a reference distribution length for the application. For the present work, this length has been taken as the aircraft wing span.

The power specific masses of the generation, management, and distribution systems and the power specific fuel mass flowrate for a generator

system were estimated using engineering equipment supplier information in the public domain coupled with simple analytical physics. A summary of the key information used for this analysis is included as Table 2. One of the key unknowns in the present analysis is the estimation of the likely power specific mass of the actuator (power conversion) subsystem used for future aircraft application. A decision was made that this should be based solely on the mass/power characteristics of the piezoelectric diaphragm used in the present design of SJA and that the mass of the housing should not be included. This is justified on the basis that the housing is a relatively lightly loaded passive structure whereas the piezoelectric actuator is active and relatively highly loaded.

3 RESEARCH METHODS AND APPARATUS

3.1 Laboratory characterization of SJA technology

The primary objective of the experimental work was to measure actuator authority (velocity output) and efficiency (fluid power out divided by absorbed electrical power in) as a function of excitation voltage $V(t)$ and actuator geometry. This information can then be used to identify optimal actuator configuration/excitation with respect to authority and efficiency for use as part of the systems application study. Note that in practice actuator authority and efficiency may also be dependent on the values of various dimensionless parameters related to fluid flow within the actuator, including Reynolds number, Strouhal number, Stokes number, and Mach number [**10**–**12**]. It is proposed that the work presented here is valid on the basis that, firstly, the actuator geometry and operating conditions are reasonably close to those expected for industrial application and, secondly, that the effects of variation of the dimensionless fluid flow parameters due to geometry changes are likely to be small compared with the effects of variation of device Helmholtz frequency due to geometry changes.

The SJA design used for the present study is based on a cylindrical chamber bounded by a vibrating diaphragm driven by a piezoceramic [**15**] actuator (Fig. 2). Note that for this configuration, the orifice is opposite the diaphragm. In practice, if the largest chamber dimension is smaller than a quarter of the acoustic wavelength at the frequency of operation, then the time-varying pressure within the chamber is spatially uniform and the orifice may be placed at any location in the wall of the chamber.

A schematic illustrating the power flow through a piezoceramic driven SJA is shown in Fig. 3. This system is well suited to analysis via a lumped element modelling (LEM) approach, and has been studied in this way by a number of previous authors [**5**]. From the theory of dynamic systems, it can be inferred that maximum power will be transferred through the system when the real component of impedance for each of the subsystems is a minimum and the reactive components are equal, i.e. each subsystem is operated at resonance. For the present experiments, a commercially sourced brass disc/piezo patch actuator is used to provide the electromechanical aspects of the system. Since these actuators are reasonably

Table 2 Specifications of selected hardware and power specific mass parameters used for the case study analysis

Power generation	
Reference	Auxiliary power unit (APU): Honeywell 36–300
Fuel consumption (maximum load)	125 kg/h
Power rating and weight	291 kW and 140 kg
Power specific mass m_{W_g}	≈ 0.5 kg/kW
Energy storage	
APU fuel consumption rate $\dot{m}_{W_g}$	≈ 0.5 kg/kW h
Power management	
Reference	Electronic amplifier: Apex Microtechnology (PA52 + EK27)
Maximum power/mass	100 V (single end) and 40 A = 4 kW, 0.5 kg
Power specific mass m_{W_m}	≈ 0.13 kg/kW
Power distribution	
High power cable reference	Pro power tri rated (RS)
Maximum transmissible power	600 V (single end) and 100 A = 60 kW
Power specific mass per unit length m'_{W_d}	$3 \times 10 - 3$ kg/kW m
Power specific mass based on aircraft wing span (34 m) m_{W_d}	≈ 0.1 kg/kW
Power conversion	
Reference	Commercial PZT disc actuator, FT-27T-3.9A1
Max. absorbed power/mass	5 W/1.5 g
Power specific mass m_{W_c}	≈ 0.3 kg/kW
Overall power specific mass $m_{W_g} + m_{W_m} + m_{W_d} + m_{W_c}$	≈ 1 kg/kW

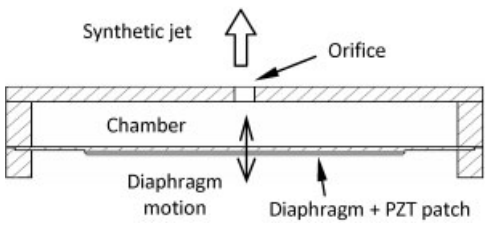

Fig. 2 Cross-sectional view of a synthetic jet actuator

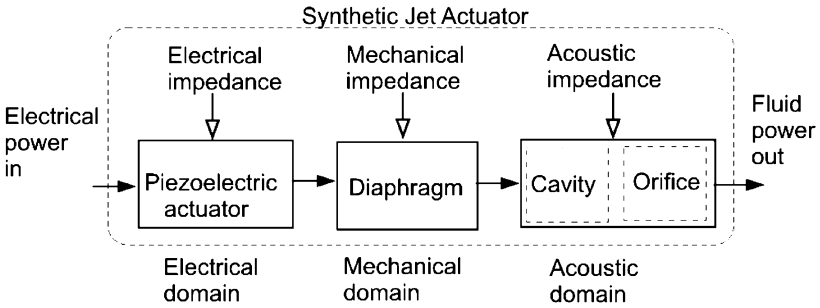

Fig. 3 Power flow through a piezoceramic driven SJA

optimized for acoustic applications, the present system is primarily concerned with the matching between the diaphragm mechanical impedance and the acoustic impedance of the cavity.

The chamber dynamics are typically dominated by the associated Helmholtz mode [**16**], for which the resonant frequency is given by

$$f_{\mathrm{H}} = \frac{c}{2\pi}\sqrt{\frac{S}{Vh}}\,(\mathrm{Hz}) \tag{17}$$

where S is the cross-sectional area of the orifice, h is the orifice depth, V is the cavity volume, and c is the speed of sound. Since the orifice geometry is typically fixed by fluid mechanics constraints, the choice of cavity volume is the primary means by which a designer can influence the matching between diaphragm and chamber, and hence influence the maximum power flow through the actuator. Therefore, the primary geometric variable in the present experimental work is the chamber volume, which, for a fixed chamber diameter, is directly proportional to the chamber height.

3.2 Experimental apparatus

A modular SJA prototype was manufactured allowing a systematic variation of chamber and orifice heights (Fig. 4). It is composed of three modules: a base ring, a chamber ring, and an orifice disc. The base ring is a single piece containing a lip in the inner edge of its top side to locate the PZT diaphragm and to provide a clamping surface. Several chamber rings and orifice discs were manufactured such that the chamber and orifice heights could be systematically varied. Six equispaced bolts were used to provide a uniform clamping load on the PZT diaphragm.

The chamber diameter was constrained by the availability of commercially sourced piezoceramic actuators and was fixed at 25 mm. This diameter was also consistent with a number of previous experiments [**4**, **5**]. The orifice diameter was fixed at 1.2 mm, giving a chamber-to-orifice diameter ratio of around 20, which is similar to that used by other researchers [**17**–**21**] (though there is limited evidence to suggest that this ratio is important).

The piezoelectric disc used for the present investigation was obtained from APC International Ltd (FT-27T-3.8A1). It was composed of a single piezoelectric patch bonded to a brass shim. The shim and patch diameter were 27 mm and 20 mm respectively. The thickness of both was ≈ 0.22 mm, giving a total diaphragm thickness of ≈ 0.44 mm. The overall mass of the disc is 1.5 g.

The actuator excitation signal was generated using a Thurlby Thandar TG1010A signal generator connected to a PC via an RS232 interface. The signal was amplified up to ± 350 V using a Trek Piezo Driver/Power Amplifier Model PZD350. This amplifier provides monitor channels for low-voltage representation of the high-voltage output and load current

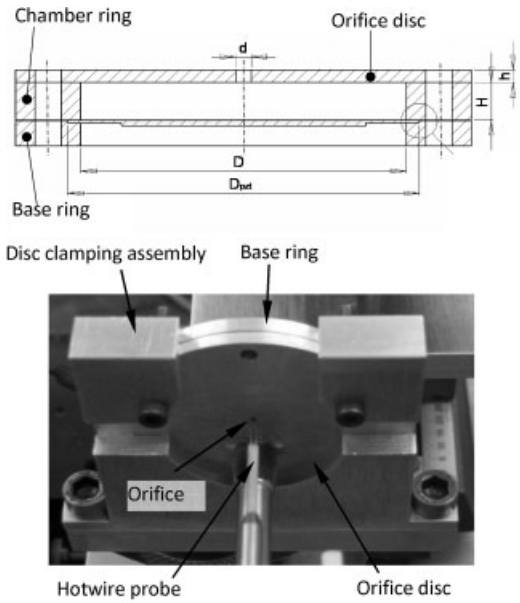

Fig. 4 Scale drawing and photograph of the modular SJA experimental apparatus

sensing for power measurement purposes. Sinusoidal excitation was used for all the tests conducted.

Jet velocities were measured under quiescent external flow conditions with a hot-wire anemometry system composed of a Dantec 55P11 hot-wire probe (width = 1.2 mm) and a TSI IFA 100 intelligent flow analyser. The probe was positioned in line with the orifice centre-line and $1D_o$ away from the orifice exit plane, as shown in Fig. 5.

The probe used has the same width as the orifice diameter, which means that the probe effectively measures an average of the instantaneous velocity profile $1d$ downstream of the orifice exit [**22**]. While this is not an ideal way of measuring the mean jet velocity, it is highly repeatable and it is proposed that the level of precision is consistent with the overall objectives of the study.

The hot-wire was calibrated using a DISA 55D41 venturi meter with a maximum velocity capability of 160 m/s. Accuracy decreases with increasing velocity up to ± 4 m/s at maximum calibration speed. Temperature compensation [**23**] was incorporated in the hot-wire measurements, E, by correcting the hot-wire bridge voltage, E_b, according to the relationship

$$E = E_b \sqrt{\frac{T_w - T_c}{T_w - T_e}} \tag{18}$$

where T_w is the temperature of the wire under quiescent conditions, T_c is the ambient temperature at time of calibration, and T_e is the ambient temperature at the time of data collection. The frequency response of the hot-wire anemometer unit is 250 kHz, allowing a maximum sampling of 60 points in a 4 kHz jet cycle.

The calibration process involved recording velocity and hot-wire voltage in incremental steps for the entire velocity range, resulting in an array of typically 35 points (i.e. 1 point every 5 m/s). The calibration was implemented as a fifth-order polynomial.

As part of broader actuator model validation objectives outside the scope of this paper, the actuator rig was also instrumented for measurement of chamber pressure and diaphragm displacement. These measurements are not specifically needed for evaluation of actuator authority and efficiency, but they do add to an understanding of the physics associated with these parameters. An example set of data from the SJA rig is shown in Fig. 6. Note that for this case, the diaphragm peak velocity is around 0.5 m/s (calculated from the time derivative of displacement). Assuming a mean peak 'piston' velocity of half this value, the conservation of mass gives an exit velocity of around 100 m/s (based on a diaphragm-to-orifice area ratio of 343 and incompressible flow). This is of a similar order of magnitude to the experimentally observed peak velocity of around 60 m/s, though note that the peak jet velocity occurs approximately 45° *ahead* of the peak diaphragm velocity. Note also for reference that the peak diaphragm amplitude of 25 μm is relatively small compared to the chamber height for the configuration tested (approximately 4 per cent).

3.3 Experimental method

The test matrix dimensions for the present set of experiments are given in Table 3. In order to maximize experimental productivity, only selected regions of the test matrix were investigated in detail. The procedure adopted was as follows. Firstly, a coarse mapping of the result space was undertaken to define regions of potential interest and to check that the acquisition set-up was fit for the purpose. Next, a nominally optimal value of the orifice depth was identified over the frequency range of interest, with the chamber depth and excitation amplitude

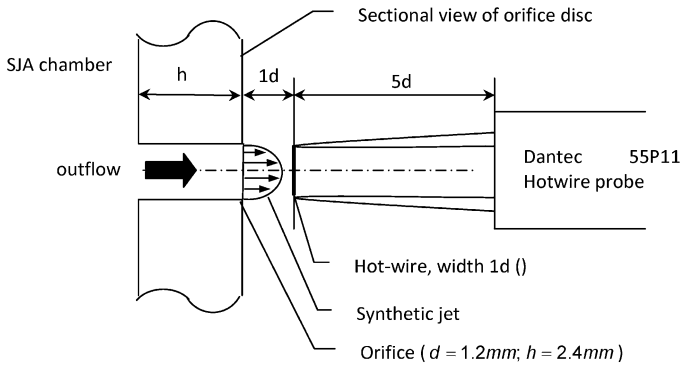

Fig. 5 Hot-wire size and position with respect to the SJA orifice exit

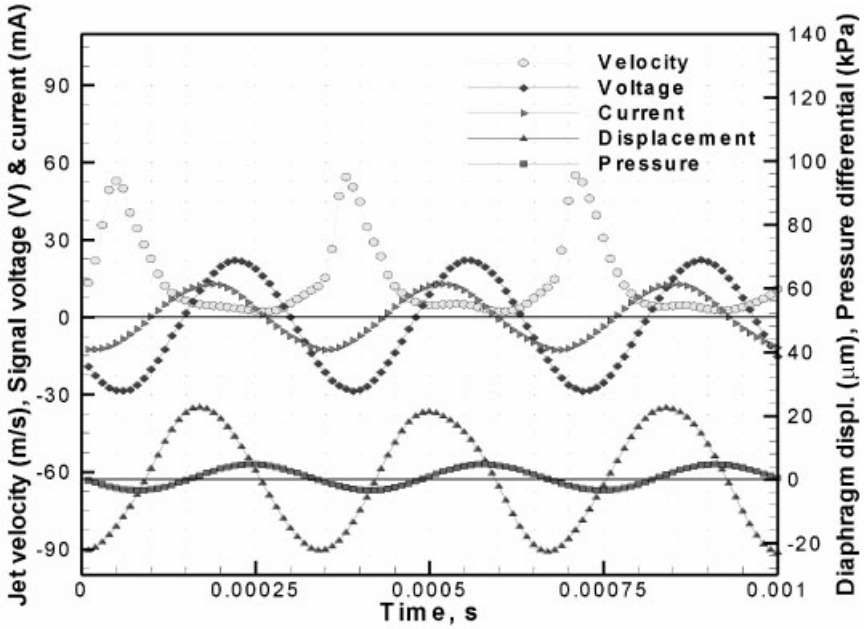

Fig. 6 Example of stream of data recorded when actuator was operating at 3 kHz and $V_o = 50$ V (actuator geometry settings: $h/d = 2.1$, $H/d = 0.56$)

fixed. After this, an optimal value of the chamber depth was identified for the nominally optimal orifice height and fixed excitation amplitude. Finally, the geometry with optimized orifice depth and chamber depth was characterized over the full range of excitation amplitude and frequency.

An experimental method was required that enabled simultaneous measurements of actuator excitation voltage, excitation current, and hot-wire output voltage. Furthermore, this process should be automated with respect to varying the demanded excitation voltage and frequency, such that actuation characterization data sets could be obtained in a time-efficient manner. The solution adopted involved the use of a two-computer master–slave arrangement. The master computer ran an experimental control program that was able to generate actuator excitation signals and send acquisition control signals to the slave computer. Acquisition was performed using LabView installed on the slave computer. The overall data acquisition scheme is shown in Fig. 7.

All data were sampled at 100 kHz, with 20 k samples taken for each data point (sample window of 0.2 s). At the highest excitation frequency of 4 kHz, this provided a minimum of 25 samples per cycle and a data point ensemble average based on 800 cycles. At the lowest excitation frequency (50 Hz) data point ensemble averaging takes place over approximately 10 cycles.

3.4 Case study analysis for example aircraft

The aim of the case study analysis is to generate understanding of how the flight conditions and location of the flow control application affect the SJA system overall mass and power requirement. The aircraft chosen for the case study is an A320 (mass 75 tonnes, 150 passengers, range 2500 nm) (Fig. 8). This aircraft class was chosen on the basis that it historically represents the best selling sector in terms of number of units sold in the Airbus range of civil transport aircraft. Further specifications are presented in Table 4. Table 5 details further information on the flight profile considered for the case study analysis.

Three different case study scenarios were developed based around low-speed (take-off/landing) and

Table 3 Definition of test matrix dimensions

Experimental variable	Range	Number of intervals
Excitation frequency	0–4 KHz	80
Excitation amplitude V_o	0–250 Vpp (peak-to-peak)	13
Orifice depth-to-diameter ratio h/d	0.6–4.2	10
Chamber depth-to-orifice diameter ratio H/d	0.5–5.8	14

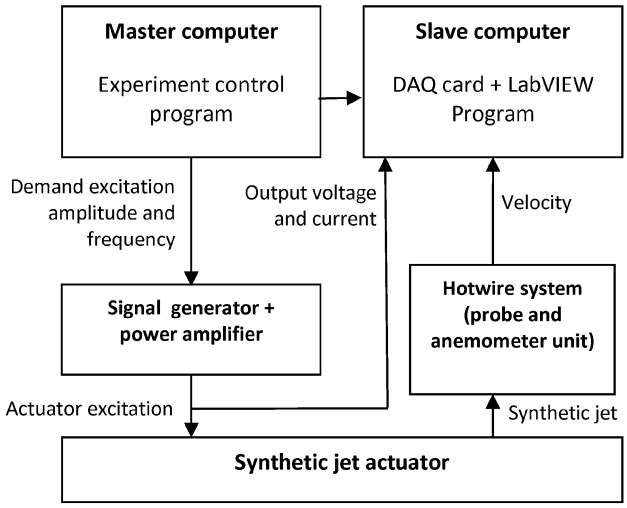

Fig. 7 Schematic diagram of experiment control and data acquisition system

high-speed (cruise) flight conditions. For the low-speed case, the design objective is improvement in high lift performance through enhanced boundary layer mixing on the slat and on the flap. For the high-speed case, the objective is reduction in wave drag through shock control in a similar way to that investigated by Brunet *et al.* using vortex generators [**28**]. It should be recalled that the purpose of this study is evaluation of the cost of implementing an SJA-based flow control system based on established guidelines; the benefits, e.g. reduced drag and increased maximum lift, are not considered.

The power requirement of an SJA application as defined in section 2 and by equation (9) depends critically on the local flow conditions. For the present case study, this information was derived from publicly available pressure data for a generic Airbus aerofoil section in low-speed [**28**] and high-speed [**29**, **30**] configurations, as shown in Fig. 9. It was decided that for the slat and flap flow control scenarios, a single row of SJAs would be applied at the quarter-chord location of each of the elements. This location is a reasonable choice on the basis that it is within the region of strong adverse pressure gradient downstream of the leading edge suction

Fig. 8 The A320 aircraft used for the case study

Table 4 A320 aircraft specification [**24**–**26**]

Aircraft type	A320-200
Maximum take-off mass	75 000 kg
Cruise altitude	8 500 m
$M_{\text{TO/landing}}$	0.2
M_{Cruise}	0.874
Mean aerodynamic chord (MAC)	4.29 m
Wing semi-span b	17 m
Wing area	123 m^2

peak where separation is likely to occur. Furthermore, the quarter-chord location is typically the thickest part of the aerofoil and thus provides most volume for actuator installation, which may be a critical constraint in practice. For the high-speed scenario, the chosen actuator location is just ahead of the normal shock on the upper surface of the main element.

The geometric, aerodynamic, and operational parameters required as inputs into the system model for the three case study scenarios are defined in Table 6. Note that it is assumed that the flow control system on the flap and slat is used for take-off, initial climb, approach, and landing (total operation time of 10 minutes per flight). The sonic local velocities for the slat and main element cases create an issue that sonic jet actuator velocities are required to achieve the target of a velocity ratio of 1. While it has not been possible to demonstrate SJA velocities this high in the laboratory (and compressibility effects are likely to make this very challenging), the case studies assume that sonic jet velocities are achievable.

4 RESULTS

4.1 SJA characterization and optimization

This section will present a summary of the experimental results from the actuator optimization study, leading to identification of a velocity-optimized

Table 5 Typical flight profile for regional operation of an A320 [**24**–**27**]

	Duration	
Flight phase	min	%
Taxi	12	10.0
Take-off	1	0.8
Initial climb	2	1.7
Climb	15	12.5
Cruise	68	56.7
Descent	15	12.5
Approach	5	4.2
Landing	2	1.7
Total	120	100.0

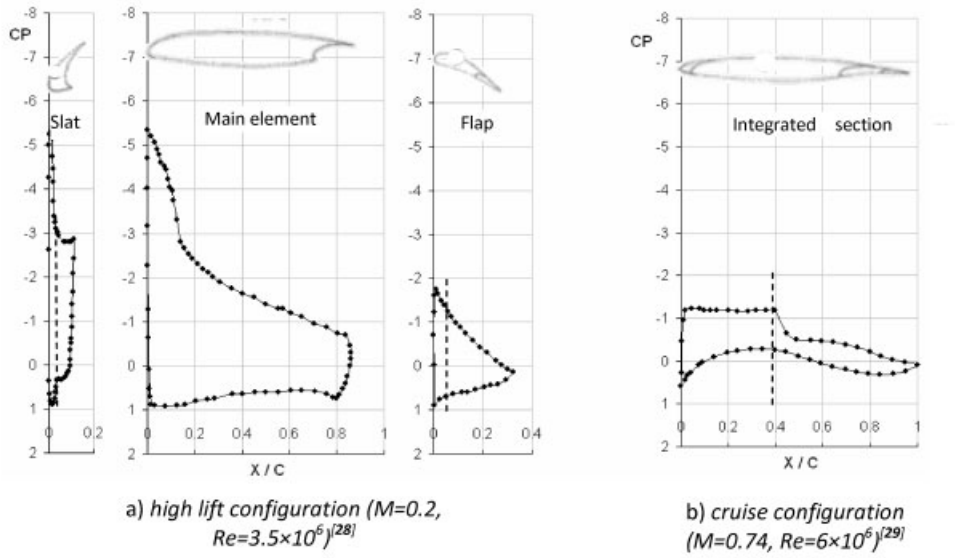

Fig. 9 Experimental pressure distribution around a generic Airbus type airfoil section. Actuator location used for case studies indicated by dashed line

actuator that will be used as the basis of the case study evaluation in section 4.2.

The effect of changing chamber height on the velocity obtained from the actuator as a function of excitation frequency is shown in Fig. 10. This figure is for an excitation amplitude of 110 V; however, the frequency response is approximately independent of excitation amplitude (as will be discussed later with reference to Fig. 13). Comparison of the theoretically predicted chamber natural frequency with the observed frequencies at which velocity is maximized shows that the experimental results are consistent with the underlying model discussed in section 3.1. For large chamber heights, the chamber resonance is at a much lower frequency than the diaphragm resonance and there is little interaction between the chamber and diaphragm modes. As the chamber height is reduced, the observed chamber resonant frequency approaches the diaphragm natural frequency and the velocity peak obtained at the diaphragm natural frequency increases significantly. Note that the diaphragm natural frequency also increases with decreasing chamber height. This is due to the increased contribution of the chamber volume to the diaphragm stiffness.

A drawing of the actuator in the $H/d = 0.56$ configuration is shown in Fig. 11. It is worth noting that the high chamber aspect ratio identified as optimal in the present work is inconsistent both with the geometry used for many experimental [**2**, **3**, **4**, **8**–**11**] and CFD [**31**–**33**] related studies of SJA actuator performance and the schematic diagrams typically used by researchers to illustrate the operation of SJAs.

Quantitative data for the actuator peak velocity as a function of excitation frequency for three specific chamber heights are shown in Fig. 12. The $H/d = 2.0$ case represents the 'unoptimized' actuator geometry

Table 6 Definition of geometric, aerodynamic, and operational parameters used for the three case study scenarios

	Chordwise location of actuator array		Spanwise extent of actuator array		Local free stream conditions at actuator chordwise location				
Flow control scenario	*% chord*	*Dimensional value**	*% semi-span*	*Total deployed span*	*Local Mach number*	*Velocity*	*Density*	*Boundary layer height**	Duration of operation
(a) Slat	25% slat chord	0.47 m	91%	15 m	1	340 m/s	1.2 kg/m^3	2 mm	10 min
(b) Flap	25% flap chord	1.29 m	73%	12 m	0.45	150 m/s	1.2 kg/m^3	4 mm	10 min
(c) Main element	40% combined section chord	4.29 m	91%	15 m	1	300 m/s	0.5 kg/m^3	14 mm	68 min

* At spanwise location of MAC.

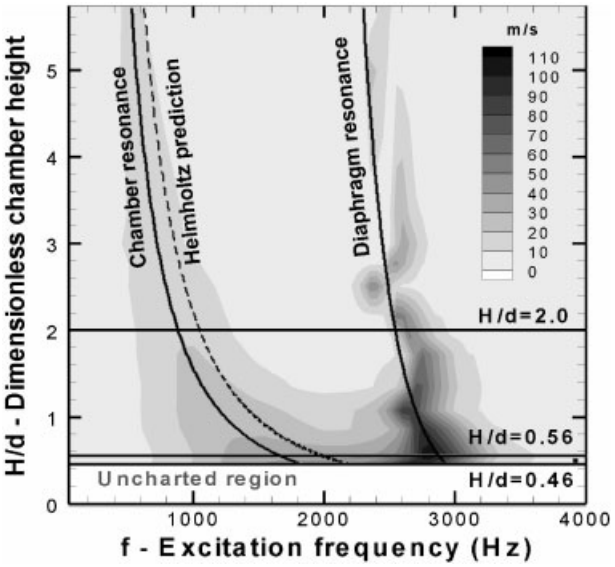

Fig. 10 Characterization of SJA peak velocity as a function of excitation frequency for varying chambers

used for a number of previous studies within the laboratory [**3**, **4**] and the peak velocity obtained is around 50 m/s. The $H/d = 0.56$ case represents the 'optimized' geometry from the present set of experiments and the peak velocity at approximately 110 m/s is double that achieved for the unoptimized case. Note that for the unoptimized case there are two distinct peaks in the velocity frequency response, whereas for the optimized case the peaks have substantially merged.

Velocity output data for the optimized actuator geometry for a complete excitation amplitude–frequency sweep are shown as a contour plot in Fig. 13, with velocity slices at the chamber and diaphragm resonant frequencies reproduced in Fig. 14. The maximum velocity obtained from the actuator increases monotonically with the excitation amplitude, reaching a peak of 130 m/s at the maximum excitation amplitude of $V_o = 250$ V used for the present experiments. Further increases in excitation amplitude lead to electromechanical damage of the diaphragm. Figure 13 shows that the form of the velocity frequency response for the actuator is essentially independent of excitation amplitude, which would be expected for a reason-

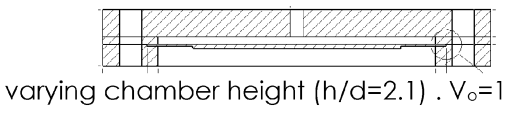

Fig. 11 Cross-sectional view of the velocity optimized synthetic jet actuator

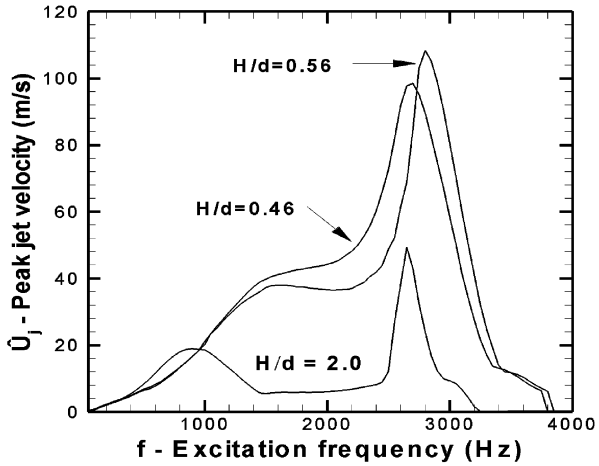

Fig. 12 SJA peak velocity response as a function of excitation frequency for $H/d = 0.56$, 0.60, and 2.0 ($h/d = 2.1$); $V_o = 110$ V

ably linear dynamic system. The velocity amplitude, however, is not a linear function of excitation amplitude. There are two main reasons for this. Firstly, from power considerations, it would be expected that excitation amplitude (power input) would be proportional to velocity cubed (output power). Secondly, it is likely that the piezoceramic material is saturating at higher voltages, bearing in mind the actuators used are specified for a nominal operating voltage of around $V_o = 30$ V. Measurement of the diaphragm peak displacement at a high excitation voltage ($V_o = 250$ V) shows that this is of the order of 75 μm, which is well within the expected linear stiffness region of the diaphragm, so this is unlikely to contribute towards saturation. There are non-linear fluid dynamic losses due to compressi-

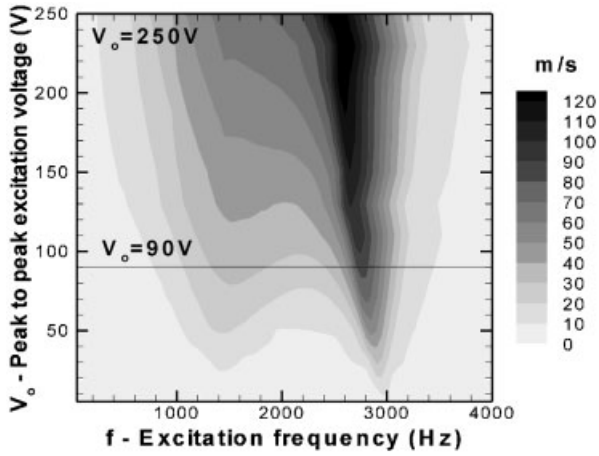

Fig. 13 Characterization of SJA peak velocity output as a function of excitation frequency for varying excitation voltages ($h/d = 2.1$ and $H/d = 0.56$)

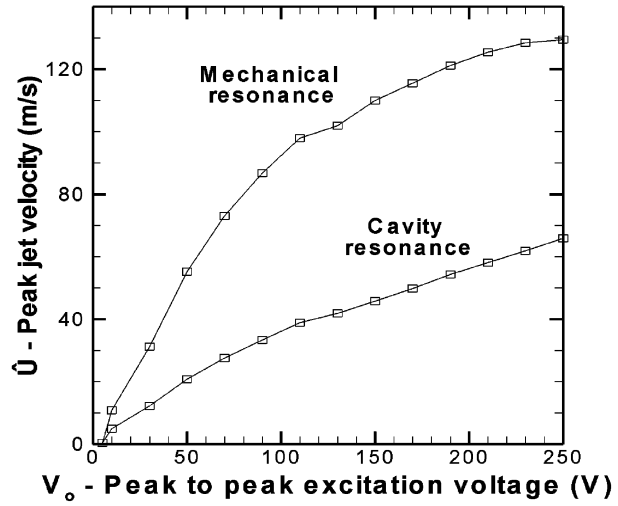

Fig. 14 SJA peak velocity response as a function of excitation frequency at resonant frequencies ($h/d = 2.1$ and $H/d = 0.56$)

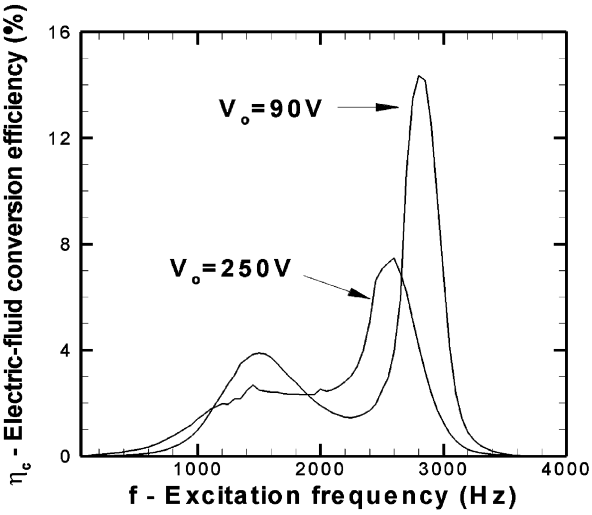

Fig. 16 SJA electric–fluid conversion efficiency as a function of excitation frequency for $V_o = 90$ V and $V_o = 250$ V ($h/d = 2.1$ and $H/d = 0.56$)

bility and viscous effects as the flow discharges through the orifice, but it is not possible to quantify these at the present time.

A map of the electrical-to-fluidic power conversion efficiency of the actuator is shown in Fig. 15, with slices at excitation amplitudes corresponding to peak efficiency and peak velocity shown in Fig. 16. There are two regions of increased efficiency associated with the diaphragm and chamber resonances and these map on to the regions of peak velocity identified in Fig. 13.

A peak efficiency of around 14 per cent is obtained at a peak-to-peak (pp) excitation amplitude of 90 V and excitation frequency of 2.8 kHz, corresponding to a velocity of 70 m/s. As the peak-to-peak excitation amplitude increases above 120 V, the efficiency reduces, decreasing to a value of 7 per cent at the peak velocity output condition, i.e. $V_o = 250$ V. The non-collocation of conditions of peak velocity output and peak efficiency is consistent with the general problem of dielectric saturation of the piezoelectric patch discussed in section 3.1. Recent experiments with piezoelectric diaphragms of the same diameter but different thickness have shown an increase in peak jet velocity up to 200 m/s with an efficiency of 10 per cent. It is plausible therefore to consider a power conversion efficiency of 10 per cent for the case study analysis that follows.

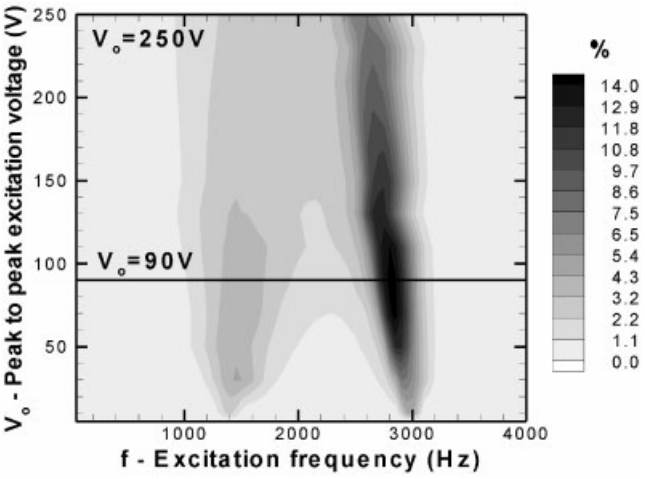

Fig. 15 Electric–fluidic conversion efficiency as a function of excitation amplitude and frequency for the velocity-optimized actuator geometry ($h/d = 2.1$ and $H/d = 0.56$)

4.2 Case study

An important output from the present work is the development of understanding of the relative importance of the mass cost of power generation, management, distribution, and conversion components of an SJA-based flow control system. This can be approached in the first instance by comparison of the power specific masses of each of the subsystems (Fig. 17). Based on the model parameters used for the present study, for a given fluid power requirement, approximately one-third of the mass cost of the overall system is due to the mass of the actuators themselves and approximately half of the cost is due to the provision of power generation capacity. Power distribution and management subsystems then contribute approximately equally to the remaining sixth of the overall cost.

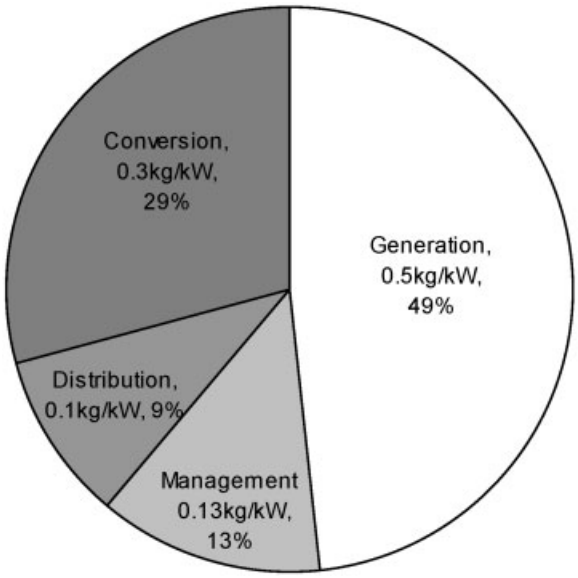

Fig. 17 Comparison of the relative mass costs of power generation, management, distribution, and conversion for an SJA-based flow control system on an A320 class aircraft

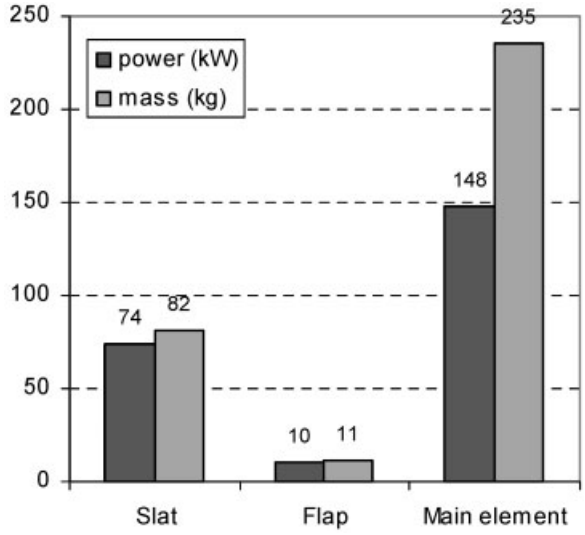

Fig. 18 Comparison of overall required power and overall mass for the three case study scenarios

One of the key parameters driving the present analysis is the actuator power conversion efficiency, and it is instructive to consider how the overall system of mass and power is affected by the achieved value. Considering the relative mass contribution between subsystems first, a 10 per cent increase in power conversion efficiency will lead to a 10 per cent reduction to the power specific mass of the actuators, all other power specific masses remaining unchanged. However, the overall power required by the system will be reduced by 10 per cent, and thus the overall mass is reduced by this much, plus a smaller gain (e.g. +3 per cent) due to the relatively reduced actuator mass. From the foregoing, it is clear that actuator power conversion efficiency is critical in driving the mass efficiency of the overall system. Given the relatively low value of 10 per cent achieved during the present optimization study, it is clear that there are considerable benefits to be had from pursuing more efficient actuator designs.

Attention will now be focused on the quantitative estimates for the flow control system mass and power requirements. These are estimated using a combination of the case study definition in Table 6, the hardware data in Table 2, and the empirical flow control rules discussed in section 2. The output from this analysis is shown in Table 7, with a comparison of key values given in Fig. 18.

The absorbed electrical power varies considerably between each of the case study scenarios. The main factor affecting the relative power between applications is the required jet velocity. Both the slat and main element require approximately double the jet velocity of the flap application and, since power is proportional to velocity cubed, approximately eight times the power. The main element has fewer actuators than the slat, but the overall aggregate area is approximately three times as large as for the slat, and this accounts for the increased power requirement.

Table 7 Case study results: estimated values for electrical power and system mass for the slat, flap, and main element flow control system applications

Flow control scenario	Actuator orifice diameter (mm)	Total number of actuators	Mean fluid power output (kW)	Absorbed electrical power (kW)	Mass (kg)					Total mass (kg)
					Generation	Management	Distribution	Conversion	Fuel	
(a) Slat	0.4	7500	7.4	74	37.0	9.6	6.7	22.2	6.2	81.7
(b) Flap	0.8	3000	1	10	5.1	1.3	0.9	3.1	0.8	11.2
(c) Main element	2.8	1070	14.8	148	74.1	19.3	13.3	44.5	84.0	235.2

By the nature of the way in which the flow control system is modelled, the trends in overall system mass follow the trends in power required. The relative masses of the generation, management, distribution, and conversion subsystems for each of the case study scenarios are fixed by the ratios of power specific masses and hence are the same for each case. The fuel mass, however, depends on the duration of operation of the system and hence the fuel mass for the main element case (cruise) is a larger proportion of the overall mass than for the slat and flap cases, explaining the corresponding decrease in the overall power-to-mass ratio for the main element flow control system.

In order to put quantitative values of power in context, the typical auxiliary power unit (APU) found on an A320 class aircraft is rated at around 300 kW. This means that the slat, flap, and main element flow control systems would require 25, 3, and 50 per cent of the APU power output respectively. On the basis that the APU is conventionally not used during flight, then use of an existing APU for flow control applications may offset some of the associated mass cost. However, note that the reliability/redundancy level of current APU systems would have to be improved if they were to be used for flight-critical systems such as high lift. This would increase the mass and reduce possible gains from 'dual' use for flow control.

With regard to the values of system mass, the slat and flap systems both contribute around 2000 kg to the mass of the wing of an A320 class aircraft. The slat and flap flow control systems thus represent around 4 and 0.6 per cent of the existing mechanical systems weight. The mass of the slat flow control system corresponds to a delta C_L value of 0.0002 at take-off conditions. This value represents the minimum delta C_L benefit obtained from implementing a slat flow control system required for the system to break even from a systems mass perspective.

5 CONCLUSIONS

This paper has attempted to move the civil transport flow control debate forward by considering the power and mass cost of implementing electrically operated synthetic jet actuators for three specific flow control tasks on an A320 aircraft. The study has involved (a) the development of a low-order mass model based on estimated power specific masses of generation, management, distribution, and conversion subsystems, (b) application of existing empirical rules for successful application of pneumatic boundary layer mixing flow control devices to determine required fluid power for the case study applications, and (c) characterization and optimization of lab-based SJA technology to establish realistic estimates for power conversion efficiency and actuator maximum authority.

Specific conclusions from the laboratory-based SJA work are as follows.

1. The peak velocity obtained from a velocity-optimized synthetic jet actuator was 130 m/s, at an excitation amplitude and frequency of 250 V_{pp} and 2.6 kHz respectively. The power conversion efficiency at this condition was 7 per cent.
2. The best power conversion efficiency achieved with the velocity-optimized actuator was 14 per cent. This occurred at an excitation amplitude and frequency of 90 V and 2.8 kHz respectively. The velocity output at this condition was 70 m/s.
3. Velocity output and power conversion efficiency of the actuator are both maximized when the natural frequency of the chamber is matched with the diaphragm natural frequency, and the actuator is excited at this frequency. This is consistent with what would be expected from dynamic systems theory.

Specific conclusions from the A320 case study analysis are as follows.

4. The mass cost of an energy-based flow control system needs to include the mass cost of generating, managing, distributing, and converting electrical power and the mass cost of the energy used to provide that power over a given operation time.
5. The two main power specific mass costs for the case study considered here are generation (50 per cent) and conversion (30 per cent). The power specific mass for the overall flow control system considered for the A320 application is estimated to be around 1 kg of system mass per kW of electrical power required.
6. The mass and power requirements for the A320 slat, flap, and main element case study scenarios are 74 kg, 82 kW; 10 kg, 11 kW; and 148 kg, 235 kW respectively. The relatively long duration of the main element (cruise) scenario means that the mass cost due to energy is significantly larger for this case compared to the slat and flap cases.
7. The slat, flap, and main element flow control systems would require 25, 3, and 50 per cent of the power output of the typical existing APU on an A320, respectively, and around 4 and 0.6 per

cent of the existing mechanical systems weight associated with a slat or flap, respectively.

ACKNOWLEDGEMENTS

The authors would like to thank Airbus UK and BAE Systems for their financial and technical support to this work, through the CAFEDA (Control of Aerodynamic Flows for the Environmentally Driven Aircraft) programme and other sponsored work at the University of Manchester.

REFERENCES

1 **Bieler, H., Abbas, A., Chiaramonte, J.,** and **Sawyers, D.** Flow control for aircraft performance enhancements – overview of Airbus – University cooperation. In 3rd AIAA Flow Control Conference, San Francisco, California, 2006, paper AIAA 2006-3692.

2 **Glezer, A.** and **Amitay, M.** Synthetic jets. *Annual Rev. Fluid Mechanics*, 2002, **34**.

3 **Crook, A.** *The control of turbulent flows using synthetic jets*. PhD dissertation, The School of MACE (Mechanical Aerospace and Civil Engineering), The University of Manchester, 2002.

4 **Liddle, S. C., Crowther, W. J.,** and **Wood, N. J.** Investigation of phase and spacing effects in synthetic jet actuator arrays. In 43rd AIAA Aerospace Sciences Meeting and Exhibit, Reno, Nevada, 2005.

5 **Gallas, Q., Holman, R., Nishida, T., Carrol, B., Sheplak, M.,** and **Cattafesta, L.** Lumped element modelling of piezoelectric-driven synthetic jet actuators. *Am. Inst. Aeronaut. Astronaut. J.*, 2003, **41**(2).

6 **Schaeffer, N.** The interaction of a synthetic jet and a turbulent boundary layer. In 41st Aerospace Sciences Meeting and Exhibit, Reno, Nevada, 2003, paper AIAA 2003-0643.

7 **Gomes, L., Crowther, W.,** and **Wood, N.** Towards a practical piezoelectric diaphragm based synthetic jet actuator for high subsonic applications – effects of chamber and orifice depth on actuator peak velocity. In 3rd AIAA Flow Control Conference, San Francisco, California, 2006, paper AIAA-2006-2859.

8 **Yehoshua, T.** and **Seifert, A.** Boundary condition effect on oscillatory momentum generators. In 33rd AIAA Fluid Dynamics Conference, Orlando, Florida, 2003, paper AIAA 2003-3710.

9 **Jabbal, M.** and **Zhong, S.** The near wall effect of synthetic jets in a laminar boundary layer. In 3rd AIAA Flow Control Conference, San Francisco, 2006, paper AIAA 2006-3180.

10 **Guo, F.** and **Zhong, S.** A PIV investigation of the characteristics of micro-scale synthetic jets. In 3rd AIAA Flow Control Conference, San Francisco, California, 2006, paper AIAA 2006-3183.

11 **Milanovic, I.** and **Zaman, K.** Synthetic jets in crossflow. *Am. Inst. Aeronaut. Astronaut. J.*, 2005, **43**(5), 929–940.

12 **Holman, R., Utturkar, Y., Mittal, R., Smith, B.,** and **Cattafesta, L.** Formation criterion for synthetic jets. *Am. Inst. Aeronaut. Astronaut. J.*, 2005, **43**(10), 2110–2115.

13 **Hepperle, M.** JavaFoil – analysis of airfoils. Online software, cited 22 October 2007; URL: http://www.mh-aerotools.de/airfoils/javafoil.htm.

14 **Houghton, E. L.** and **Carpenter, P. W.** *Aerodynamics for engineering students*, 4th edition, 1993, 368 pp. (Butterworth-Heinemann, Oxford).

15 *Piezoelectric ceramics: principles and applications*, 2006, pp. 17–19 (APC International Ltd).

16 **Hersh, A. S.** and **Walker, B.** Fluid mechanical model of the Helmholtz resonator. NASA paper CR-2904, 12 pp.

17 BS EN ISO 5167–2, Measurement of flow by means of pressure differential devices inserted in circular cross-section conduits running full – Part 2: orifice plates, 2003.

18 **Miller, R. W.** *Flow measurement engineering handbook*, 1983 (McGraw-Hill, New York).

19 **Ward-Smith, A. J.** Critical flowmetering: the characteristics of cylindrical nozzles with sharp upstream edges. *Int. J. Heat and Fluid Flow*, 1979, **1**(3).

20 **Grace, H. P.** and **Lapple, C. E.** Discharge coefficients for small-diameter orifices and flow nozzles. *Trans. Am. Soc. Mech. Engrs*, 1951, **73**, 639–647.

21 **Kayser, J. C.** and **Shambaugh, R. L.** Discharge coefficient for compressible flow through small-diameter orifices and convergent nozzles. *Chem. Engng Sci.*, **46**(7), 1671–1711.

22 **Uchida, S.** The pulsating viscous flow superposed on the steady laminar motion of incompressible fluid in a circular pipe. *Z. Angew. Math. Phys.*, **7**, 403–422.

23 **Brunn, H. H.** *Hot-wire anemometry: principles and signal analysis*, 1995, pp. 208–212 (Oxford Science Publications).

24 **Jackson, P.** *Jane's all the world aircraft 2004–05*, 2005.

25 **Mathews, C.** *Aeronautical engineering's data book*, 2002, pp. 124, 125 and 138–143 (Butterworth-Heinemann, Oxford).

26 **Jenkinson, L., Simpkin, P.,** and **Rhodes, D.** Civil jet aircraft design, data sets. Online database, cited 22 August 2007; URL: http://www.apnet.com/companions/034074152X/appendices/default.htm.

27 Airbus Customer Service, Getting to grips with fuel economy. *Flight Operations Support and Line Assistance,* Issue 3, 2004.

28 **Brunet, V., Francois, C., Garnier, E.,** and **Pruvost, M.** Experimental and numerical investigations of vortex generators effects. In 3rd AIAA Flow Control Conference, San Francisco, California, 2006, paper AIAA 2006-3027.

29 **Wedderspoon, J.** The high lift development of the A320 aircraft. AGARD CP-515, 1993, p. 31.

30 **Greff, E.** The development and design integration of variable camber wing for long/medium range aircraft. *Aeronaut. J.*, 1990.

31 **Yao, C. S., Chen, F. J., Neuhart, D.,** and **Harris, J.** Synthetic jets in quiescent air. In Proceedings of NASA LaRC Workshop CFD Validation of Synthetic Jets and Turbulent Separation Control, Williamsburg, Virginia, 2004.

32 **Garnier, J. D.** and **Sagaut, P.** DNS/LES of active separation control by synthetic jets. In 3rd AIAA Flow Control Conference, San Francisco, USA, 2006, paper AIAA 2006-3026.

33 **Tang, H.** and **Zhong, S.** Development of a prediction model for synthetic jets in quiescent conditions. In 43rd AIAA Aerospace Sciences Meeting and Exhibit, Reno, Nevada, 2005, paper AIAA 2005-0104.

APPENDIX

Notation

A	area (m^2)
b	wing semi-span (m)
c	speed of sound (m/s)
C_L	lift coefficient
C_p	pressure coefficient
d	orifice diameter (m)
D_o	chamber diameter (m)
E	hot-wire voltage (V)
f	frequency (Hz)
h	orifice depth (m)
H	chamber depth (m)
I	current (A)
ℓ	orifice spacing (m)
l	reference distribution length (m)
m	mass (kg)
M	Mach number
n	number of actuators
Re	Reynolds number
s_A	spanwise extent (m)
S	orifice area
t	time (s)
T	period (s) or temperature (K)
U	speed (m/s)
V	voltage (V) or cavity volume (m^3)
V_R	velocity ratio
W	power (W)
x	distance (m)
δ	boundary layer thickness (m)
Δ	ratio of orifice diameter to local boundary layer height
Δt	duration (s)
η	efficiency
λ	ratio of actuator spanwise spacing to orifice diameter
ν	kinematic viscosity (m^2/s)
ρ	density (kg/m^3)
ω	angular velocity (rad/s)

Subscripts

b	bridge
c	conversion, or ambient calibration
Ch	chemical
d	distribution
e	ambient present
E	electrical
f	fluid
F	fluidic
g	generation
H	Helmholtz
j	jet
L	local
m	management
o	amplitude
w	wire
W	power

Embellishments

$\hat{x}$	peak
$\dot{x}$	time derivative
$\bar{x}$	mean
x'	per unit length

Abbreviations

APU	auxiliary power unit
MAC	mean aerodynamic chord
nm	nautical miles
pp	peak-to-peak
PZT	lead zirconate titanate
SJA	synthetic jet actuator
TO	take-off